



Effect of thermal residual stresses on matrix failure under transverse tension at micromechanical level. A numerical and experimental analysis

E. Correa, V. Mantič, F. París

► To cite this version:

E. Correa, V. Mantič, F. París. Effect of thermal residual stresses on matrix failure under transverse tension at micromechanical level. A numerical and experimental analysis. Composites Science and Technology, 2011, 71 (5), pp.622. 10.1016/j.compscitech.2010.12.027 . hal-00730306

HAL Id: hal-00730306

<https://hal.science/hal-00730306>

Submitted on 9 Sep 2012

HAL is a multi-disciplinary open access archive for the deposit and dissemination of scientific research documents, whether they are published or not. The documents may come from teaching and research institutions in France or abroad, or from public or private research centers.

L'archive ouverte pluridisciplinaire **HAL**, est destinée au dépôt et à la diffusion de documents scientifiques de niveau recherche, publiés ou non, émanant des établissements d'enseignement et de recherche français ou étrangers, des laboratoires publics ou privés.

Accepted Manuscript

Effect of thermal residual stresses on matrix failure under transverse tension at micromechanical level. A numerical and experimental analysis

E. Correa, V. Mantič, F. París

PII: S0266-3538(10)00495-1
DOI: [10.1016/j.compscitech.2010.12.027](https://doi.org/10.1016/j.compscitech.2010.12.027)
Reference: CSTE 4892

To appear in: *Composites Science and Technology*

Received Date: 31 August 2010
Revised Date: 17 December 2010
Accepted Date: 18 December 2010



Please cite this article as: Correa, E., Mantič, V., París, F., Effect of thermal residual stresses on matrix failure under transverse tension at micromechanical level. A numerical and experimental analysis, *Composites Science and Technology* (2010), doi: [10.1016/j.compscitech.2010.12.027](https://doi.org/10.1016/j.compscitech.2010.12.027)

This is a PDF file of an unedited manuscript that has been accepted for publication. As a service to our customers we are providing this early version of the manuscript. The manuscript will undergo copyediting, typesetting, and review of the resulting proof before it is published in its final form. Please note that during the production process errors may be discovered which could affect the content, and all legal disclaimers that apply to the journal pertain.

Effect of thermal residual stresses on matrix failure under transverse tension at micromechanical level. A numerical and experimental analysis.

E. Correa, V. Mantić, F. París

Group of Elasticity and Strength of Materials, School of Engineering, University of Seville

Camino de los Descubrimientos S/N, 41092 Sevilla, Spain

Tel: 34 954 48 72 99; Fax: 34 954 46 16 37

e-mail: correa@esi.us.es, mantic@esi.us.es, paris@esi.us.es

Abstract. In the present work the influence at micromechanical scale of thermal residual stresses, originated in the cooling down associated to the curing process of fibrous composites, on inter-fibre failure under transverse tension is studied. In particular, the effect of the presence of thermal residual stresses on the appearance of the first debonds is discussed analytically, whereas later steps of the mechanism of damage, i.e. the growth of interface cracks and their kinking towards the matrix, are analysed by means of a single fibre model and making use of the Boundary Element Method. The results are evaluated applying Interfacial Fracture Mechanics concepts. The conclusions obtained predict, at least in the case of dilute fibre packing, a protective effect of thermal residual stresses against failure initiation, the morphology of the damage not being significantly affected in comparison with the case in which these stresses are not considered. Experimental tests are carried out, the results agreeing with the conclusions of the numerical analysis.

Keywords: B. Curing; B. Debonding; C. Modelling; C. Transverse cracking; Micromechanics.

1. INTRODUCTION

The final stage of the manufacturing process of fibrous composites materials is the curing of the material. The differences in free contraction between the fibres and the matrix cause, during this stage of the process, the appearance of thermal residual stresses. These residual stresses are generated at micromechanical level for unidirectional and multidirectional laminates, and also at macro/meso-mechanical level for multidirectional laminates. Additionally, extra residual stresses may arise in thermosetting matrix composites from chemical shrinkage of the matrix as it cures. The presence of these stresses may affect the strength of the laminate and also have influence on the development of failure mechanisms in the material.

The study of residual stresses at macro- and meso-mechanical level is widely developed, there being several methods able to quantify them, Andersson et al. [1]. By contrast, at micromechanical level, the measurement and prediction of residual stresses presents more difficulties, due to the high complexity of the material at this scale. If knowledge of the mechanisms of failure at micromechanical level is considered to be fundamental for the development of failure criteria able to perform a more complete diagnosis of the appearance of these mechanisms, Paris [2], the analysis of the influence of curing stresses at this scale then becomes highly relevant.

Many authors have tried to quantify the effect of residual curing stresses of fibre reinforced composites leading to relevant conclusions. Particularly, Crasto and Kim [3] measured the differences in free expansion of $0^\circ/90^\circ$ laminates cured at different temperatures, and later in [4] analysed, for the case of unidirectional laminates, the influence of curing time on the generation of residual stresses. Huang and Young [5] carried out several fragmentation tests comparing interfacial shear strength between materials cured at 80°C and at room temperature, finding higher values of interfacial shear strength for the material cured at 80°C . De Kok and Meijer [6] performed transverse loading tests at temperature different from the room one, showing that residual stresses have a protective effect against failure, this effect increasing with fibre content (according to [7] these results were already presented by De Kok in his doctoral dissertation in 1995).

The particular case of inter-fibre failure (also known as matrix failure) under transverse tension has already been the object of several micromechanical studies by the authors, Paris et al. [8, 9], for single fibre case or dilute packing. These studies have made it possible to understand the initiation of failure at the micromechanical scale as well as its later progress, which leads to the macro-failure of the material, without considering the presence of residual curing stresses. The results obtained assumed that crack nucleation is controlled by the radial stress generated between fibre and matrix and showed that the maximum values are placed, in the single fibre case (or dilute packing), at the angles 0° and 180° with respect to the tension applied, Fig. 1a. Once a small debonding crack is supposed to appear (in particular, one of 10° length centred at 0° was assumed, which later proved to be in accordance with the range predicted by Mantič [10]), single-fibre BEM models, similar to that shown in Fig. 2a, were employed for the characterisation of crack growth. The results produced by the BEM model, analysed following the energetic approach of Interfacial Fracture Mechanics, predicted an unstable growth of the interface crack up to a position characterized by debonding angle $\theta_d = 60^\circ\text{--}70^\circ$, Fig. 1b. The study also showed that the end of unstable growth coincides with the development of a physically relevant contact zone

at the crack tip. The third step of the analysis, Fig. 1c, ascertained the condition under which the interface crack would find it easier to kink into the matrix than to continue growing along the interface, a problem studied with the BEM model showed in Fig. 2b. The coalescence of these kinked cracks caused the appearance of a macromechanical failure which, as expected and confirmed from the experiments [9], was oriented perpendicularly to the external load.

Some authors have employed FEM models to numerically analyse the role of residual stresses in transverse failure. In this sense, Asp et al. [7] performed FEM analyses to study the transverse failure, finding that the presence of residual stresses delays the initiation of failure in composites with a high fibre content. Fiedler et al. [11] concluded that thermal residual stresses lead to an increase in transverse strength with the local fibre-volume fraction. Zhao et al. [12] claimed that for tension dominated transverse loading, residual stress could be detrimental or beneficial depending on the material strength. Specifically, residual stresses seem to be detrimental for relatively low resin strength and beneficial for relatively high resin strength. Hojo et al. [13] performed FEM analyses for two dimensional image-based models, concluding that microscopic thermal residual stresses contribute greatly to the increase in transverse strength. Maligno et al. [14] studied the effect of residual stresses on uniaxial transverse failure using a non-uniform cell model, finding that they provide a general beneficial effect.

The present work is a continuation of the previous studies of the authors related to inter-fibre failure under transverse tension [8, 9]. The objective now is to analyse the influence of thermal residual stresses originated by the cooling down associated to the curing process on the conclusions obtained so far about the different micromechanical phases of mechanism of damage. The numerical predictions derived from Boundary Element analyses are validated with macromechanical experimental tests.

Particularly, in Section 2 the main features of the BEM model employed as well as the materials properties are presented. Sections 3, 4 and 5 are referred to the study of the initiation and growth of a crack at the interface between a fibre and the matrix surrounding it, subjected to the combined action of an external traction and the thermal decrease associated to the cooling down of a curing process. Section 6 includes the results associated to the experimental tests carried out on specimens subjected to different curing cycles. Finally, in Section 7, a discussion on the connection between numerical and experimental results is presented.

2. SINGLE FIBRE MODEL

The numerical study has been carried out using a tool based on BEM, París and Cañas [15], that makes it possible to perform the numerical analysis of plane elastic problems considering contact and interface cracks, in a similar way to that described in Blázquez et al. [16] for planar problems and Graciani et al. [17] for axisymmetric problems. Two BEM models are used in this analysis. The basic model employed is shown in Fig. 2a and represents the case of a crack which, under the plain strain hypothesis, grows along the interface symmetrically to axis 2 (Section 4). Due to this symmetry it is only necessary to study one half of the problem. As an indication, the number of boundary elements modelling the fibre is 83 and that corresponding to the matrix is 115. A strongly refined BEM mesh toward the crack tip is applied. The size of the smallest element located at the crack tip is $7 \cdot 10^{-7} a$, a being the fibre radius, in order to achieve very high accuracy in the numerical results obtained. This small size of the elements, far away from the zone where a continuum theory can be applied, is used to guarantee accurate results at distances where continuum theory is applicable.

To characterize the problem from the Fracture Mechanics point of view the energy release rate, G , will be used. The expression employed, based on the VCCT, Irwin [18], for a circular crack that propagates from a certain debonding angle, θ_d , Fig. 2a, to $\theta_d + \Delta\theta_d$ ($\Delta\theta_d \ll \theta_d$), is:

$$G(\theta_d, \Delta\theta_d) = \frac{1}{2\Delta\theta_d} \int_0^{\Delta\theta_d} \left[\sigma_{rr}(\theta_d + \theta) \Delta u_r(\theta_d - \Delta\theta_d + \theta) + \sigma_{r\theta}(\theta_d + \theta) \Delta u_\theta(\theta_d - \Delta\theta_d + \theta) \right] d\theta \quad (1)$$

where θ is the circumferential coordinate with reference to axis 2, Fig. 2a. σ_{rr} and $\sigma_{r\theta}$ represent, respectively, radial and shear stresses along the interface, and Δu_r and Δu_θ represent the relative displacements of the crack faces. Both modes of fracture, I (associated to σ_{rr}) and II, (associated to $\sigma_{r\theta}$), are obviously considered in Eq. (1). For this study the value of $\Delta\theta_d$ employed has been 0.5° .

When the presence of an incipient crack in the matrix is considered, Section 5, the previous model is altered to represent the case of a crack that has first grown along the interface and, once kinked into the matrix, is progressing through it, Fig. 2b. The materials chosen for the analysis included in Sections 3, 4 and 5 correspond to a typical configuration among fibre reinforced materials: a glass fibre-epoxy matrix system, with additional calculations for a graphite-epoxy system being necessary for the discussion in Section 7; properties of the three materials used are included in Table 1. The fibre radius considered has been $a = 7.5 \cdot 10^{-6} m$.

Dimensionless results for G will be presented, being then no significant the fact that the fibre radius consider is, strictly speaking, only adequate for glass fibre. These values are obtained, following Toya [19] and Murakami [20], by dividing the values of G by $G_0 = (1 + \kappa^m / 8\mu^m) \sigma_0^2 a \pi$, where $\kappa^m = 3 - 4\nu^m$, μ^m is the shear modulus of the matrix and σ_0 denotes the value of the applied tension.

Finally, the curing process used for the matrix considered in this work (epoxy resin) commonly consists of a first stage at room temperature followed by one or more stages at higher temperature. Independently of the temperature at which the curing process takes place, the contraction of the matrix (always higher than that of the fibre) dominates the generation of thermal residual stresses. This fact allows the inclusion of thermal residual stresses in the analysis to be modelled by means of an adequate temperature decrease that captures the real curing contraction of the material. In the present work a longitudinal transverse contraction of 0.4% has been considered, corresponding to an 80°C decrease.

3. ORIGIN OF THE DAMAGE

The beginning of the inter-fibre failure under transverse tension is considered to be controlled by the radial stress that acts at the fibre-matrix interface, under the hypothesis (not always corresponding exactly to reality) of an initially undamaged material. If the external tension is the only load considered, it can be verified [9] that the zones of maximum radial stress, and therefore susceptible of housing the first debonds, are located at $\theta = 0^\circ, 180^\circ$. Thus, the analysis of the effect of thermal residual stresses on the initiation of failure must be carried out under the same premise, studying the distribution of stresses around the interface when the fibre-matrix system suffers a thermal decrease corresponding to the curing contraction of the matrix. The consideration of real curing parameters, as detailed in Section 2, unavoidably leads to the choice of σ_0 corresponding to failure values. In particular, based on Soden et al. [21], the transverse tensile strength of the unidirectional laminate chosen for the bimaterial system considered has been $Y_T = 35 \text{ MPa}$.

In this situation, an analysis of the stress state in a single fibre-configuration, assuming the interface to be initially in perfect condition and considering a temperature decrease of 80 °C as a single solicitation, would allow the order of the thermal residual stresses to be estimated and their effect on the initiation of damage predicted.

The problem presented in these terms can be solved analytically (plane problem of a fibre embedded in an infinite matrix) and the solution obtained, Annex A, shows that residual stresses are

only produced in the radial direction, σ_{rr} , and angular direction, $\sigma_{\theta\theta}$. These stresses are proportional to the thermal decrease and only depend on the radial coordinate. Besides, σ_{rr} presents a compressive character and maintain a constant value for the whole interface, this value being determined by the following equation:

$$\sigma_{rr}^{(int)} = \Delta T G^M \frac{E^M \alpha^M (1 - 2\nu^F)(G^F + \lambda^F) - E^F \alpha^F (1 - 2\nu^M)(G^M + \lambda^M)}{(1 - 2\nu^M)(1 - 2\nu^F)(G^M + \lambda^M)(G^M + \lambda^F + G^F)} \quad (I.16)$$

For the bi-material system under consideration the value obtained is $\sigma_{rr} = -10 \text{ MPa}$.

The thermal residual compressive radial stresses detected at the interface would inhibit the appearance of the inter-fibre failure, since they involve an apparent additional strength having to be surmounted by the stress state to produce the first debonds, though their location would not be altered. In any case, comparing the residual stress level (-10 MPa) with the transverse tensile strength (35 MPa) it can be deduced that, though of the same order, the stress due to the external load is dominant.

4. THE INTERFACE CRACK

The presence of compressive thermal residual stresses provides the interface with additional protection against the initiation of damage, as has been explained in the previous section. In any case, once the failure is initiated it is also necessary to analyse the influence of thermal residual stresses over the growth of the first debonds. To this end the model appearing in Fig. 2a is used in this section to carry out, by means of the BEM, an analysis of the interface crack growth under the combined action of an external tensile load ($\sigma_0 = Y_T$) and a thermal decrease of 80 °C.

The results obtained, in terms of G versus the debonding angle θ_d , are presented in Fig. 3 for the case under study (named as $\Delta T = -80^\circ \text{C}$ in the Figure), which considers both thermal residual stresses and those derived from the load σ_0 , and for the case of single action of σ_0 ($\Delta T = 0^\circ \text{C}$ in the Figure), used as a reference in this analysis and a basis for the conclusions presented in [9].

The evolutions observed for both cases are similar, not only for the global value G but also for the modes distribution, though lower values in all evolutions are obtained for the $\Delta T = -80^\circ \text{C}$ case. This result makes it possible to also predict a protective effect of the thermal residual stresses on the interface against the evolution of the interface crack, coinciding with the defensive action against the initiation of failure already deduced in the previous section.

In spite of the apparent similarity of the evolutions associated to $\Delta T = 0^\circ\text{C}$ and $\Delta T = -80^\circ\text{C}$, the more relevant presence of Mode II for $\theta_d < 60^\circ$ stands out for the $\Delta T = -80^\circ\text{C}$ case in comparison with the $\Delta T = 0^\circ\text{C}$ case, which evidences an earlier development of the finite contact zone at the interface crack, as observed in Fig. 4 where the evolution of the contact zone versus θ_d for both cases is represented. In this sense, the appearance of the contact zone for the $\Delta T = -80^\circ\text{C}$ case specifically takes place for $\theta_d = 50^\circ$, a lower value in comparison with the $\Delta T = 0^\circ\text{C}$ case ($\theta_d = 60^\circ$). Coherently, the length of the contact zone is larger in the $\Delta T = -80^\circ\text{C}$ case than in the $\Delta T = 0^\circ\text{C}$ case, for all θ_d considered. This fact was already detected in [22].

In order to perform predictions about the interface crack growth it is necessary [23] to have an estimation of the critical value of G , G_c , which depends on the evolution of the fracture mode mixity, defined by the local phase angle, ψ_K , and therefore a function of θ_d . The law considered in this work for G_c is based on the simplified empirical proposal by Hutchinson and Suo [24]:

$$G_c(\psi_K) = G_{Ic} (1 + \tan^2(1 - \lambda)\psi_K), \quad (2)$$

where G_{Ic} is the critical value of G_c for Mode I and λ is the fracture mode sensitivity parameter.

ψ_K has been calculated following Mantić and Paris [25]:

$$\psi_K = 0.5 \arccos \left[F(\varepsilon)^{-1} \frac{G_I - G_{II}}{G_I + G_{II}} \right], \quad (3)$$

where $F(\varepsilon) = 1 + (\pi^2/3 - 2)\varepsilon^2 + O(\varepsilon^4)$, ε being the oscillatory index which, for the bi-material system employed, takes the value $\varepsilon = -0.074$.

This approach was already employed in [9] to be able to predict the growth of the interface crack for the $\Delta T = 0^\circ\text{C}$ case, making use of three different values of λ (within the range of typical values): $\lambda = 0.2, 0.25, 0.3$. In that case, due to the absence of direct experimental data, the value of G_{Ic} chosen for each λ was forced to fulfil the expression $G = G_c(\psi_K)$ for $\theta_d = 5^\circ$ (where $G(\theta_d = 5^\circ)$ has been obtained by interpolation). The results provided by the comparison between the values of G and G_c calculated in this way predicted an unstable growth of the interface crack up to θ_d in the range 60° - 70° .

The same process has been implemented in the present work for the case including the presence of the thermal residual stresses, $\Delta T = -80^\circ\text{C}$. First of all, the evolution of $\psi_K(G)$, calculated from Eq. (3), is presented in Fig. 5. The earlier development of a finite contact zone at the crack tip for the $\Delta T = -80^\circ\text{C}$ case versus the $\Delta T = 0^\circ\text{C}$ case, already shown in Fig. 4, is also detected

in Fig. 5 from the slightly higher values of $\psi_K(G)$ provided by the $\Delta T = -80^\circ\text{C}$ case and therefore also from the earlier reach of the 90° value, associated to pure Mode II.

The results obtained for the comparison between G and G_c are shown in Fig. 6 (G_{1c} being chosen following the same criterion previously employed for the $\Delta T = 0^\circ\text{C}$ case). The results shown in Fig. 6 predict an unstable growth of the interface crack up to θ_d in the range 50° - 70° , a similar conclusion to that already deduced for the $\Delta T = 0^\circ\text{C}$ case, though this range is wider at its lower bound. Thus, this range of termination of the unstable growth and of change in the propagation mode seems to be a favourable place for the development of a new stage of the mechanism of damage, i.e. the kinking of the interface crack towards the matrix and its propagation through it.

5. INTERFACE CRACK KINKING

The prediction of the interface crack kinking towards the matrix, once the period of unstable growth at the interface has finished, consists of two steps: the search for the preferential direction of the incipient crack in the matrix and the evaluation of the possibility of this change in the propagation of the crack.

Referring to the first aspect, the application of a kinking criterion, for instance MCS criterion (Erdogan and Sih [26]):

$$\sigma_{\theta\theta}(r, \theta_{kink}) = \max_{\theta} \sigma_{\theta\theta}(r, \theta) \quad (4)$$

in the neighbourhood of the interface crack tip within the θ_d range of termination of unstable growth, allows the most favourable direction of the incipient crack in the matrix to be predicted [9]. The application of this criterion for the $\Delta T = 0^\circ\text{C}$ case concluded that if kinking took place it would occur for $\theta_d = 60^\circ$ - 70° in a direction approximately normal to σ_0 [9,23].

The same analysis is presented here for the $\Delta T = -80^\circ\text{C}$ case, studying the circumferential stress state in the neighbourhood of the interface crack tip at the positions $\theta_d = 60^\circ$ and $\theta_d = 70^\circ$ and for points located on two circumferences (radii $r = 0.001a$ and $r = 0.01a$) centred at the tip. The numerical results are shown in Fig. 7, proving that, in accordance with the reference of the angle θ considered in the Figure, the maximum circumferential stress is produced approximately in the same direction as in the $\Delta T = 0^\circ\text{C}$ case.

With reference to the possibility of kinking taking place for the $\Delta T = -80^\circ\text{C}$ case, the energy release rate of the incipient crack in the matrix, G^m , has been calculated using the model presented in Fig. 2b and assuming the direction of the incipient crack to be perpendicular to the external

load σ_0 , in a similar way to the study previously performed in [9] for the $\Delta T = 0^\circ\text{C}$ case. This study has been carried out for different positions of the interface crack. The length of the crack in the matrix considered has been 0.013a (the minimum value permitted by the discretization employed).

The results corresponding to the $\Delta T = -80^\circ\text{C}$ case are presented in Fig. 8 jointly with the evolution of G for the interface crack (named as G^{int} in the graph), the higher level reached by G^m in comparison with G^{int} standing out here. It is also necessary to point out that the obtained G^m values correspond to Mode I, see Fig. 9, whereas G^{int} is due to Mode II, Fig. 3. The relative position of both distributions ($G^m(\theta_d)$ and $G^{\text{int}}(\theta_d)$) and the fact that in the range of termination of unstable growth of the interface crack the character of G^{int} turns into Mode II, whereas that associated to G^m corresponds to Mode I and shows unstable behaviour, see Fig. 9, favours, from an energetic point of view and in comparative terms, the possibility of crack kinking towards the matrix. Finally, taking into account that G_{lc}^m and G_{llc}^{int} in the references consulted, Correa et al. [27], provide a range of G_{lc}^m values similar, in the zone of recommended values, to those measured for G_{llc}^{int} , the possibility of kinking towards the matrix is found to be the most plausible option. This conclusion agrees with that previously obtained in [9] for the $\Delta T = 0^\circ\text{C}$ case.

6. EXPERIMENTAL RESULTS

Tension tests were planned on 90° unidirectional specimens in order to check the conclusions derived from the numerical study presented in the previous Sections. To fulfil this objective it was necessary to cure the same material at different temperatures (thus promoting a different number of thermal residual stresses) and check whether the strength of the material was affected.

The choice of a curing cycle different from that recommended by the manufacturer, but leading to a similar degree of curing, is not an easy task. Besides, not much work on this topic seems to be included in the literature. In any case, after careful and intense testing, two different curing cycles, based on [3], were selected for the manufacturing of twelve-ply unidirectional graphite-epoxy laminates:

- A) Cycle 1: Heat to 121°C in 30', hold at 121°C for 1h, heat to 177°C in 30', hold at 177°C for 3h and cool to room temperature.
- B) Cycle 2. Heat to 121°C in 30', hold at 121°C for 48h and cool to room temperature.

DMA (Dynamic mechanical analyser) is currently used to measure glass transition temperature of a laminate for the determining of its curing level. For the cases under consideration glass transition temperatures were 149 °C for the laminate cured at 121°C and 156 °C for the laminate cured at 177°C, indicating a similar curing level in both cases. This fact was confirmed by the agreement found in the Elasticity modulus of the specimens measured during the tension tests: mean values of 8507 MPa (standard deviation of 913 MPa) and 8210 MPa (standard deviation of 828 MPa), respectively, were determined for the laminates cured at 121°C and 177°C.

With reference to the strength results found in the tension tests a mean value of 38.4 MPa was obtained for the 121°C curing specimens (standard deviation of 4.9 MPa) whereas 48.6 MPa was the mean strength for the 177°C ones (standard deviation of 5 MPa). Thus, a 27% increase in strength is found for the 177°C curing specimens with reference to the 121°C ones. This result leads to the conclusion that the presence of higher residual curing stresses has a protective effect in transverse tension tests for unidirectional laminates, which is in agreement with the conclusions previously obtained from the numerical analysis.

7. DISCUSSION

As has been stated in the previous section, the conclusions derived from the experimental results obtained at macromechanical level agree with those obtained from the numerical studies performed at micromechanical level. This agreement is already a very remarkable result as, in spite of the different approaches employed in both cases (numerical and experimental), it reveals the connection existing between the micro and the macro scale.

In this section an attempt to go into this relationship in depth, trying to find quantitative connections between the micro and the macro level, is presented in the form of discussion aimed at settling the basis for the future work to be developed.

As has been explained in the introduction, the development of inter-fibre failure at micromechanical level consists of 4 different phases: nucleation of damage, interface crack growth, kinking and crack growth along the matrix. In Sections 3, 4 and 5 it has been demonstrated that the presence of curing stresses affects only the first two phases. Note that, for simplicity of the analysis, it has been tacitly assumed that the strength and fracture properties of the interface and matrix are not significantly altered by the consideration of a different curing cycle.

Consideration of the aforementioned fact led the authors to try to establish the relationship, if existent, between the experimentally measured mean strength of both groups of tested speci-

mens (associated to cycles 1 and 2 respectively) and the main parameter that has been used in this paper to evaluate the interface crack growth at micromechanical level, i.e. the energy release rate, G . Specifically, the value of G associated to the original debonding, i.e. $\theta_d = 10^\circ$, has been chosen as the representative parameter of the mechanism of damage at micromechanical level. Assuming that G depends quadratically on the load, considering superposition of mechanical and thermal load and also weak dependence of E and ν on temperature, it can be demonstrated that G as calculated from the results of the BEM code employed for a specific θ_d adjusts to the following equation:

$$G(\theta_d, \sigma_0, \bar{\alpha}, \Delta T) = G_\sigma \sigma_0^2 + G_T \bar{\alpha}^2 \Delta T^2 + G_{\sigma,T} \sigma_0 \bar{\alpha} \Delta T \quad (5)$$

where σ_0 is the external applied load, ΔT is the thermal increase considered and $\bar{\alpha}$, based on [29], is the mean value of the thermal expansion coefficient for the thermal range $\Delta T = T_1 - T_0$ considered and is calculated from:

$$\bar{\alpha}(T_0, T_1) = \frac{1}{\Delta T} \int_{T_0}^{T_1} (\alpha^m(T) - \alpha^f(T)) dT \quad (6)$$

Additionally, G_σ coefficient is the energy release rate associated to the particular debonding subjected only to unitary load, G_T coefficient is the energy release rate associated to the particular debonding subjected only to $\Delta T = 1^\circ\text{C}$ and $G_{\sigma,T}$ coefficient is the energy release rate associated to a particular debonding subjected to both effects, load and temperature, and is calculated from Eq. (5) once G_σ and G_T have previously been calculated using the BEM model.

Thus, in this case, evaluating coefficients G_σ , G_T and $G_{\sigma,T}$ for a graphite-epoxy system whose elastic properties are included in Table 1 and $\theta_d = 10^\circ$, choosing as the ranges ΔT corresponding to the maximum thermal decreases of the curing cycles considered in the previous section: Cycle 1) $\Delta T = -155^\circ\text{C}$ (cooling from $T_1 = 177^\circ\text{C}$ to room temperature, $T_0 = 22^\circ\text{C}$) and Cycle 2) $\Delta T = -99^\circ\text{C}$ (cooling from $T_1 = 121^\circ\text{C}$ to room temperature, $T_0 = 22^\circ\text{C}$), and using the mean values of $\bar{\alpha}$ associated to both thermal decreases $\Delta T = T_1 - T_0$, one $G - \sigma_0$ evolution can be computed for each curing cycle considered, as shown in Fig. 10.

From the comparison of both curves represented in Fig. 10 it can first be observed that $G(\Delta T = -155^\circ\text{C})$ reaches lower values than $G(\Delta T = -99^\circ\text{C})$ for the whole range of σ_0 considered. The consequence of this fact is clear: for the same load level the interface crack associated to the curing cycle with greater thermal decrease releases less energy than that associated to the

curing cycle with lower temperature, and thus it is farther from the failure. In particular and in order to illustrate this reasoning, if the experimentally measured value of the strength associated to cycle 2 is used, $\sigma_0(\Delta T = -99^\circ) = 38.4 \text{ MPa}$, and G is evaluated for that particular value of σ_0 but for ΔT associated to cycles 1 and 2, the results obtained are: $G(38.4 \text{ MPa}, \Delta T = -155^\circ \text{C}) = 0.934 \text{ MPa} \cdot \mu\text{m}$ (point A in Fig. 10) and $G(38.4 \text{ MPa}, \Delta T = -99^\circ \text{C}) = 1.272 \text{ MPa} \cdot \mu\text{m}$ (point B in Fig. 10). These results imply that G is 27% greater in the case of lower temperature than in the higher temperature case, and thus the closeness of failure or proximity to G_c value (assuming G_c approximately equal in both cases) would be 27% greater in the case of the cycle with lower temperature.

Focusing attention now on point C of Fig. 10 (which represents the failure situation for cycle 1, as it has been calculated considering the thermal features of this cycle and $\sigma_0 = 48.6 \text{ MPa}$, the experimentally measured strength for this cycle) and assuming again G_c as a constant, it is found that the rupture value associated to cycle 2 that can be predicted using this G_c (point D in the Figure) is $\sigma_0 = 43.8 \text{ MPa}$. Although this result reflects the previously detected qualitative experimental tendency, it does not satisfactorily approach the experimentally measured mean strength, 38.4 MPa. In the authors' view there are several causes that could be behind this difference between the experimental value and the numerical prediction.

First, the scatter detected in the experimental results. Two thick lines in grey are included in Fig. 10 parallel to the σ_0 axis, representing the range of experimental results for each group of tested specimens. It can be checked that the amplitude of these ranges is of the same order as the difference between the experimental values and the numerical predictions.

Second, the limitations of the model employed. It is possible that the single fibre model, though shown to be able to produce the most valuable information at qualitative level, proved insufficient to quantitatively connect micromechanical and macromechanical parameters. In this case multifibre models would be necessary to complete the information already obtained.

And third, it is also possible that viscoelastic effects, not considered in the model, also altered the relative position of G curves presented in Fig. 10.

Finally, another possibility to consider is that the assumed hypothesis about G_c independence of the curing cycle (i.e. independence from ΔT), and thus the assumption of equal values of this parameter for the two cases considered, did not accurately reflect the reality. In this sense, considering the Hutchinson and Suo approach (Eq. (2)) G_c would depend on G_{1c} , λ and ψ_K . With

respect to G_{1c} and λ , these parameters could depend on ΔT only if the material formed after curing were not the same in the cases considered. Referring to ψ_K , its dependence on ΔT is negligible for $\theta_d = 10^\circ$, as was shown in Fig. 5 for the glass-epoxy system. Thus, the only possibility would be that the size of the original debonding considered in the analysis ($\theta_d = 10^\circ$, i.e. 20° total length in this case) depended on the temperature of the curing cycle. The size of the debond at the onset under transverse load could not be studied only using the tools provided by the classical Fracture Mechanics, and an appropriate new approach of Fracture Mechanics, e.g. Finite Fracture Mechanics [10], would be necessary. In any case, it can be reasoned that a smaller size of the initial debonding for cycle 1 would possibly lead to a greater separation of G evolutions presented in Fig. 10 and thus to a better agreement with the experimental results at macroscale.

8. CONCLUSIONS

The numerical results obtained from single fibre models clarify, at least for the case of dilute fibre packing, the effect of residual curing stresses in the development of the inter-fibre failure under tension at micromechanical level, concluding that they have a protective effect against inter-fibre failure generation, though the phases of the mechanism of damage seem not to be significantly influenced by their presence.

The experimental results obtained from transverse tension tests, carried out on unidirectional laminates, are in agreement with the numerical results, a clear connection between micromechanical level and macromechanical level being found.

ACKNOWLEDGEMENTS

The work was supported by the Spanish Ministry of Education and Science (Projects No. TRA2005-06764, TRA2006 08077 and MAT2009-14022) and Junta de Andalucía (Projects of Excellence No. TEP-02045 and TEP-04501). The authors thank Dr. E. Graciani (University of Seville) whose BEM code has been used and Dr. A. Barroso for his assistance in the deduction of Eq. (4).

REFERENCES

- [1] Andersson B, Sjögren A, Berglund L. Micro- and meso-level residual stresses in glass-fiber/vinyl-ester composites. *Compos Sci Technol* 2000; 60: 2011-2028.

- [2] París F. A study of failure criteria of fibrous composite materials. NASA/CR-2001-210661, 2001.
- [3] Crasto AS, Kim RY. On the determination of residual stresses in fibre-reinforced thermoset composites. *J Reinf Plast Comp* 1993; 12: 545-558.
- [4] Crasto AS, Kim RY. In situ monitoring of residual strain development during composite cure. *Polymer Composites* 2002; 23(3): 454-463.
- [5] Huang Y, Young RJ. Interfacial behaviour in high temperature cured carbon fibre/epoxy resin model composite. *Composites* 1995; 26: 541-550.
- [6] De Kok JMM, Meijer HEH. Yield deformation and fracture of unidirectional composites in transverse loading. 1. Influence of fibre volume fraction and test-temperature. *Composites: Part A* 1999; 30: 905-916.
- [7] Asp LE, Berglund LA, Talreja R. Prediction of matrix-initiated transverse failure in polymer composites. *Compos Sci Technol* 1996; 56: 1089-1097.
- [8] París F, Correa E, Cañas J. Micromechanical view of failure of the matrix in fibrous composite materials. *Compos Sci Technol* 2003; 63: 1041-1052.
- [9] París F, Correa E, Mantič V. Kinking of transverse interface cracks between fibre and matrix. *J App Mech* 2007; 74(4): 703-716.
- [10] Mantič V. Interface crack onset at a circular cylindrical inclusion under a remote transverse tension. Application of a coupled stress and energy criterion. *Int J Solids Struct* 2009; 46: 1287-1304.
- [11] Fiedler B, Hojo M, Ochiai S, Schulte K, Ochi M. Finite-element modeling of initial matrix failure in CFRP under static transverse tensile load. *Compos Sci Technol* 2001; 61: 95-105.
- [12] Zhao LG, Warrior, NA, Long AC. A thermo-viscoelastic analysis of process-induced residual stress in fibre-reinforced polymer-matrix composites. *Materials Science and Engineering A* 2007; 452-453: 483-498.
- [13] Hojo M, Mizuno M, Hobbiebrunken T, Adachi T, Tanaka M, Ha SK. Effect of fiber array irregularities on microscopic interfacial normal stress state of transversely loaded UD-CFRP from viewpoint of failure initiation. *Compos Sci Technol* 2009 ; 69: 1726-1734.
- [14] Maligno AR, Warrior NA, Long AC. Effects of inter-fibre spacing on damage evolution in unidirectional (UD) fibre-reinforced composites. *European Journal of Mechanics - A/Solids* 2009; 28: 768-776.
- [15] París F, Cañas J. *Boundary Element Method. Fundamentals and Applications*. Oxford, OUP, 1997.
- [16] Blázquez A, París F, Mantič V. BEM solution of two-dimensional contact problems by weak application of contact conditions with non-conforming discretizations. *Int J Solids Struct* 1998; 35: 3259-3278.
- [17] Graciani E, Mantič V, París F, Blázquez A. Weak formulation of axi-symmetric frictionless contact problems with boundary elements. Application to interface cracks. *Comput Struct* 2005; 83: 836-855.
- [18] Irwin GR. Analysis of stresses and strain near the end of a crack transversing a plate. *J App Mech* 1957; 24: 361-364.
- [19] Toya M. A crack along the interface of a circular inclusion embedded in an infinite solid. *J Mech Phys Solids* 1974; 22: 325-348.
- [20] Murakami Y. *Stress Intensity Factor Handbook*. Oxford, Pergamon Press, UK, 1988.
- [21] Soden PD, Hinton MJ, Kaddour AS. Lamina properties, lay-up configurations and loading conditions for a range of fibre-reinforced composite laminates. *Compos Sci Technol* 1998; 58: 1011-1022.

- [22] París F, Del Caño JC, Varna J. BEM analysis of the contact problem in fibres debonded of a matrix. Effect of curing stresses. In: Kassab A, Brebbia CA, Chopra M, editors. Boundary Elements XX, Southampton, CMP, 1998.
- [23] Mantič V, Blázquez A, Correa E, París F. Analysis of interface cracks with contact in composites by 2D BEM. In: Guagliano M, Aliabadi MH, editors. Fracture and Damage of Composites. WIT Press, UK, 2006.
- [24] Hutchinson JW, Suo Z. Mixed mode cracking in layered materials. Adv App Mech 1992; 29: 63-191.
- [25] Mantič V, París F. Relation between SIF and ERR based measures of fracture mode mixity in interface cracks. Int J Fracture 2004;130: 557-569.
- [26] Erdogan F, Sih GC. On the crack extension in plates under plane loading and transverse shear. J Basic Eng 1963; 85: 519-527.
- [27] Correa E, Mantič V, París F. A micromechanical view of inter-fibre failure of composite materials under compression transverse to the fibres. Compos Sci Technol 2008; 68:2010-2021.
- [28] Noda N. Thermal stresses in materials with temperature-dependent properties. In: Hetnarski, editor. Thermal stresses I. North Holland, Amsterdam, 1986.

Annex A

Consider the plain strain problem of a single fibre embedded in an infinite matrix as shown in Figure A.1. The fibre is perfectly bonded along the interface. The whole configuration is subjected to a thermal decrease ΔT . The axial symmetry of the problem implies that $u_r = u_r(r)$, $u_\theta = 0$, $\sigma_{rr} = \sigma_{rr}(r)$, $\sigma_{\theta\theta} = \sigma_{\theta\theta}(r)$, $\sigma_{r\theta} = 0$. Equilibrium in polar coordinates for a plane elastic problem takes the following form, in view of axial symmetry and zero body forces:

$$\frac{d\sigma_{rr}}{dr} + \frac{\sigma_{rr} - \sigma_{\theta\theta}}{r} = 0 \quad (\text{A.1})$$

Expressing the components of the strain tensor ε_{rr} and $\varepsilon_{\theta\theta}$ as functions of u_r : $\varepsilon_{rr} = \frac{\partial u_r}{\partial r}$ and

$\varepsilon_{\theta\theta} = \frac{u_r}{r}$, and substituting in the constitutive law

$$\sigma_{\alpha\beta} = 2G\varepsilon_{\alpha\beta} + \lambda\varepsilon_{kk}\delta_{\alpha\beta} - \frac{E\alpha\Delta T}{1-2\nu}, \quad (\text{A.2})$$

leads to the following expressions for $\sigma_{rr}(r)$ and $\sigma_{\theta\theta}(r)$:

$$\sigma_{rr}(r) = (2G + \lambda)\frac{du_r}{dr} + \lambda\frac{u_r}{r} - \frac{E\alpha\Delta T}{1-2\nu}; \quad \sigma_{\theta\theta}(r) = (2G + \lambda)\frac{u_r}{r} + \lambda\frac{du_r}{dr} - \frac{E\alpha\Delta T}{1-2\nu} \quad (\text{A.3})$$

Introducing Eqs. (A.3) in Eq. (A.1), the following Euler's differential equation is found:

$$\frac{d^2 u_r}{dr^2} + \frac{1}{r} \frac{du_r}{dr} - \frac{u_r}{r^2} = 0 \quad (\text{A.4})$$

The solution of this equation is:

$$u_r(r) = \frac{Ar}{2} + \frac{B}{r}, \quad (\text{A.5})$$

where A and B are constants. Substituting expression (A.5) into (A.3) the stress solution of the problem raised is obtained:

$$\sigma_{rr}(r) = (G + \lambda)A - \frac{2G}{r^2}B - \frac{E\alpha\Delta T}{1-2\nu}, \quad \sigma_{\theta\theta}(r) = (G + \lambda)A + \frac{2G}{r^2}B - \frac{E\alpha\Delta T}{1-2\nu} \quad (\text{A.6})$$

The former stress solution may be particularized for both the fibre and the matrix by simply adding the superscripts F and M , respectively, obtaining:

Stress state for the fibre:

$$\sigma_{rr}^F(r) = (G^F + \lambda^F)A^F - \frac{2G^F}{r^2}B^F - \frac{E^F\alpha^F\Delta T}{1-2\nu^F}; \quad \sigma_{\theta\theta}^F(r) = (G^F + \lambda^F)A^F + \frac{2G^F}{r^2}B^F - \frac{E^F\alpha^F\Delta T}{1-2\nu^F} \quad (\text{A.7})$$

Stress state for the matrix:

$$\sigma_{rr}^M(r) = (G^M + \lambda^M)A^M - \frac{2G^M}{r^2}B^M - \frac{E^M\alpha^M\Delta T}{1-2\nu^M}; \quad \sigma_{\theta\theta}^M(r) = (G^M + \lambda^M)A^M + \frac{2G^M}{r^2}B^M - \frac{E^M\alpha^M\Delta T}{1-2\nu^M} \quad (\text{A.8})$$

It is necessary to determine the four constants involved in the former solutions: A^F , B^F , A^M and B^M . To this end the boundary conditions associated to the problem are imposed:

- For $r=0$ the stress solution of the fibre in (A.7) leads to a singularity that can only be avoided if:

$$B^F = 0 \quad (\text{A.9})$$

- For $r=R_F$ the existent adhesion at the interface between the fibre and the matrix leads to the following conditions:

$$\sigma_{rr}^M(R_F) = \sigma_{rr}^F(R_F); \quad u_r^F(R_F) - u_r^M(R_F) = 0. \quad (\text{A.10})$$

Then, substituting expressions (A.5), (A.7) and (A.8) in (A.10) yields:

$$(G^M + \lambda^M)A^M - \frac{2G^M}{R_F^2}B^M - \frac{E^M\alpha^M\Delta T}{1-2\nu^M} = (G^F + \lambda^F)A^F - \frac{2G^F}{R_F^2}B^F - \frac{E^F\alpha^F\Delta T}{1-2\nu^F} \quad (\text{A.11})$$

$$\frac{AR_F}{2} + \frac{B_F}{R_F} - \frac{AR_M}{2} - \frac{B_M}{R_F} = 0 \quad (\text{A.12})$$

- The outer boundary of the matrix is free, and thus for $r \rightarrow \infty$ the condition to be imposed is

$\sigma_{rr}^M(r \rightarrow \infty) = 0$. Using (A.8), the next expression is obtained:

$$(G^M + \lambda^M)A^M - \frac{E^M\alpha^M\Delta T}{1-2\nu^M} = 0 \quad (\text{A.13})$$

Solving the system formed by Eqs. I.11, I.13, I.14 and I.15, A^F , B^F , A^M and B^M are calculated as a function of the properties of the bimaterial system:

$$A^M = \frac{E^M \alpha^M \Delta T}{(1-2\nu^M)(G^M + \lambda^M)}, \quad B^M = -R_F^2 \Delta T \frac{E^M \alpha^M (1-2\nu^F)(G^F + \lambda^F) - E^F \alpha^F (1-2\nu^M)(G^M + \lambda^M)}{2(1-2\nu^M)(1-2\nu^F)(G^M + \lambda^M)(G^M + \lambda^F + G^F)}$$

$$A^F = \Delta T \frac{E^M G^M \alpha^M (1-2\nu^F) + E^F \alpha^F (1-2\nu^M)(G^M + \lambda^M)}{(1-2\nu^M)(1-2\nu^F)(G^M + \lambda^M)(G^M + \lambda^F + G^F)}, \quad B^F = 0$$

Finally, the stress state at the interface ($r=R_F$) is represented by:

$$\sigma_{rr}^{M(int)} = \sigma_{rr}^{F(int)} = -\sigma_{\theta\theta}^{M(int)} = \sigma_{\theta\theta}^{F(int)} = \Delta T G^M \frac{E^M \alpha^M (1-2\nu^F)(G^F + \lambda^F) - E^F \alpha^F (1-2\nu^M)(G^M + \lambda^M)}{(1-2\nu^M)(1-2\nu^F)(G^M + \lambda^M)(G^M + \lambda^F + G^F)} \quad (A.14)$$

$$\sigma_{r\theta}^{int} = 0$$

FIGURES AND TABLES

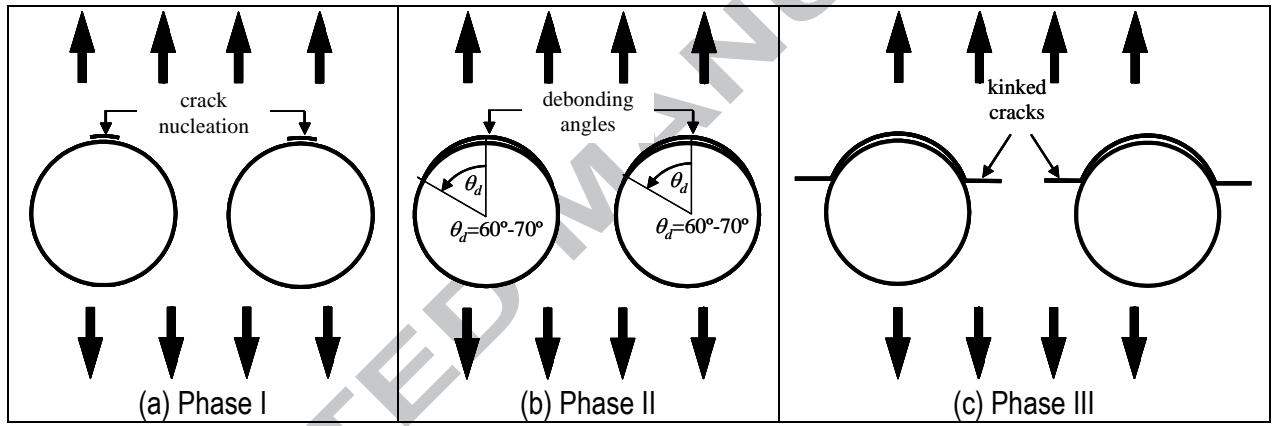


Fig. 1. Micromechanical phases of inter-fibre failure under unidirectional tension

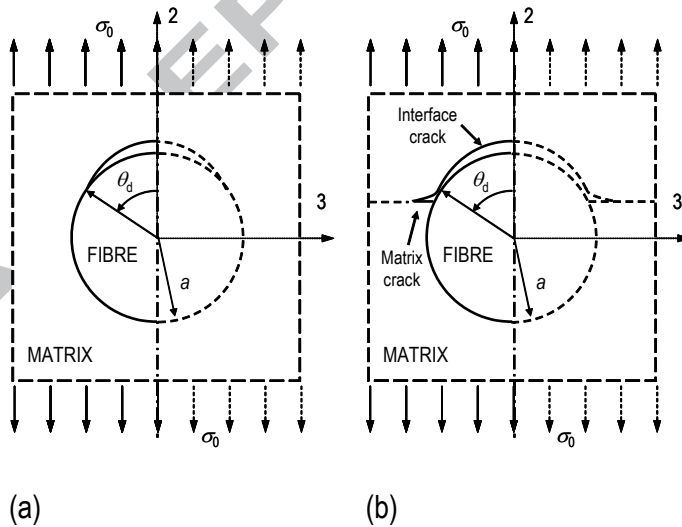


Fig. 2. Single fibre modes: a) with interface crack only, and b) with interface kinked crack

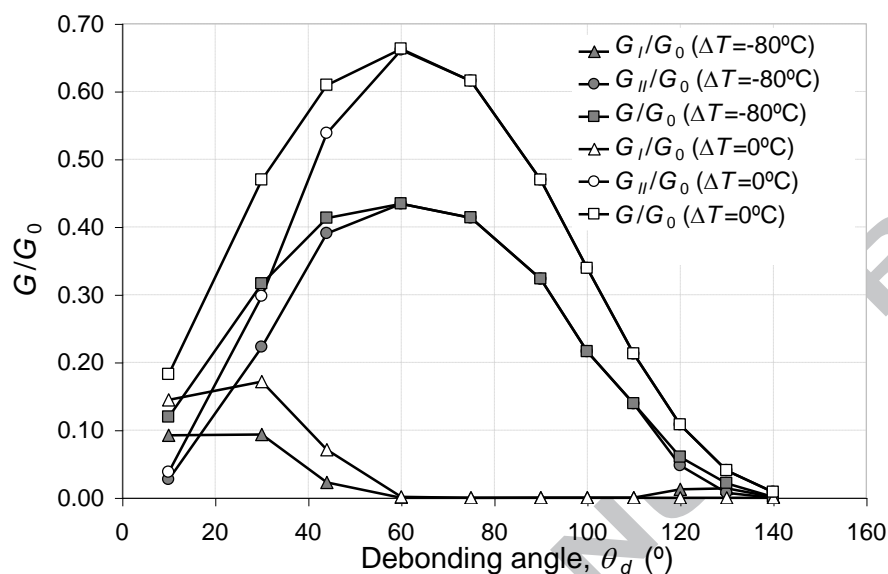


Fig. 3. G evolution versus θ_d ($\Delta T = 0^\circ\text{C}$ and $\Delta T = -80^\circ\text{C}$ cases). Glass fibre system.

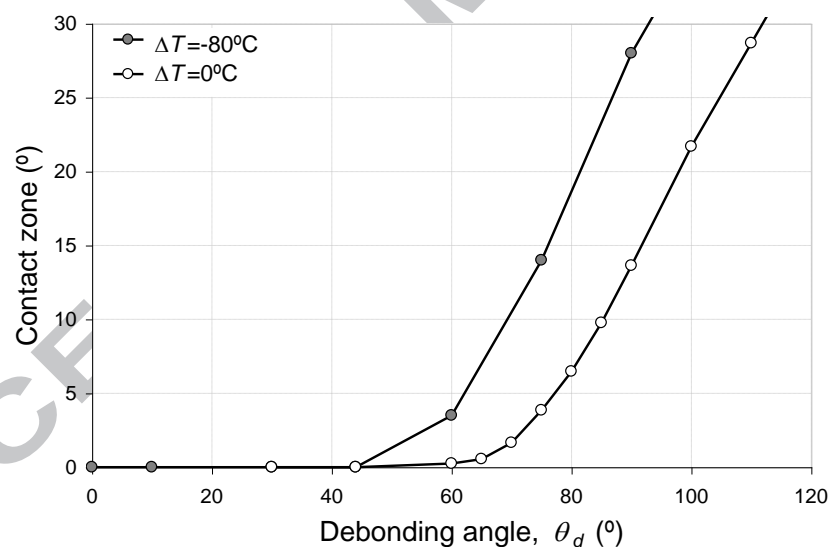


Fig. 4. Contact zone evolution ($\Delta T = 0^\circ\text{C}$ and $\Delta T = -80^\circ\text{C}$ cases). Glass fibre system.

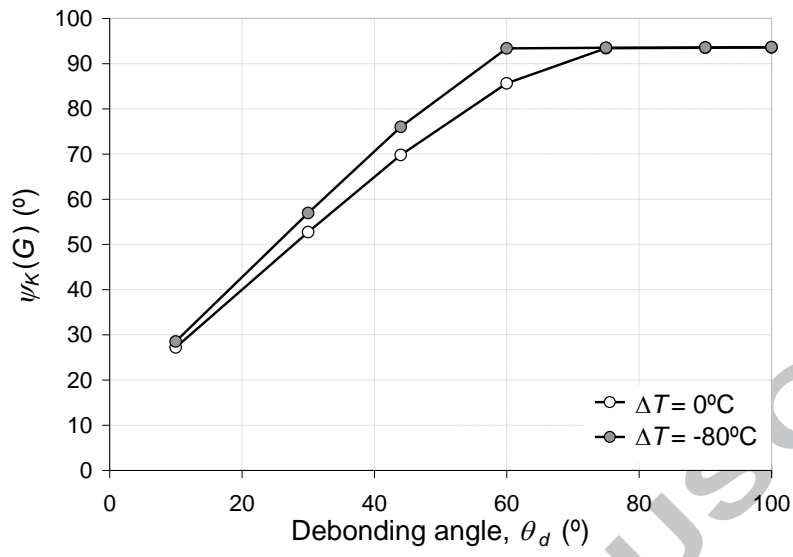


Fig. 5. $\psi_K(G)$ evolution ($\Delta T = -80^\circ\text{C}$ and $\Delta T = 0^\circ\text{C}$ cases). Glass fibre system.

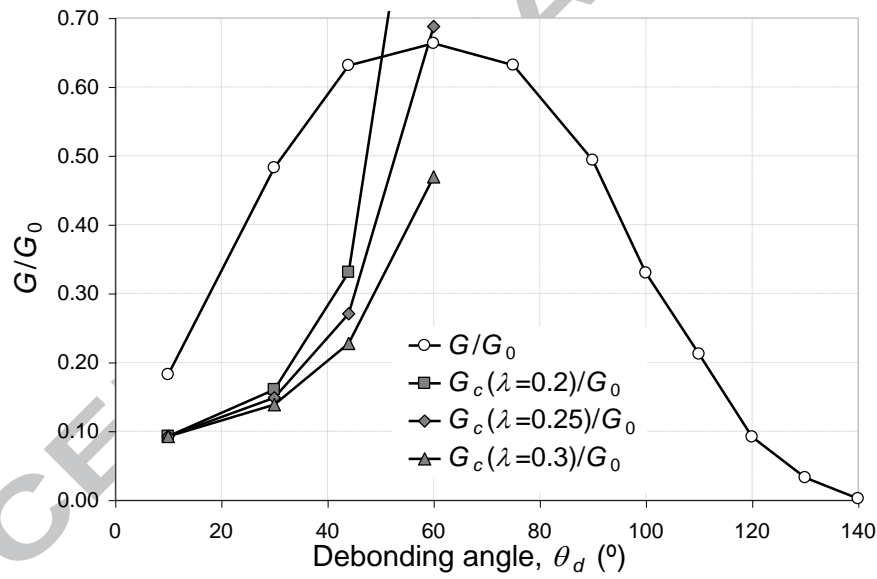


Fig. 6. G and G_c for the interface crack ($\Delta T = -80^\circ\text{C}$). Glass fibre system.

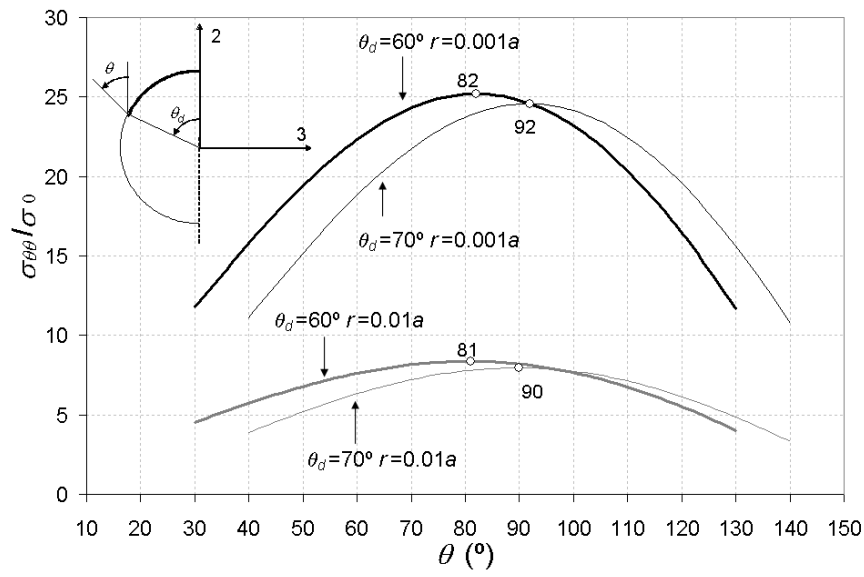


Fig. 7. $\sigma_{\theta\theta}$ distribution around interface crack tip ($\Delta T = -80^\circ\text{C}$ case). Glass fibre system.

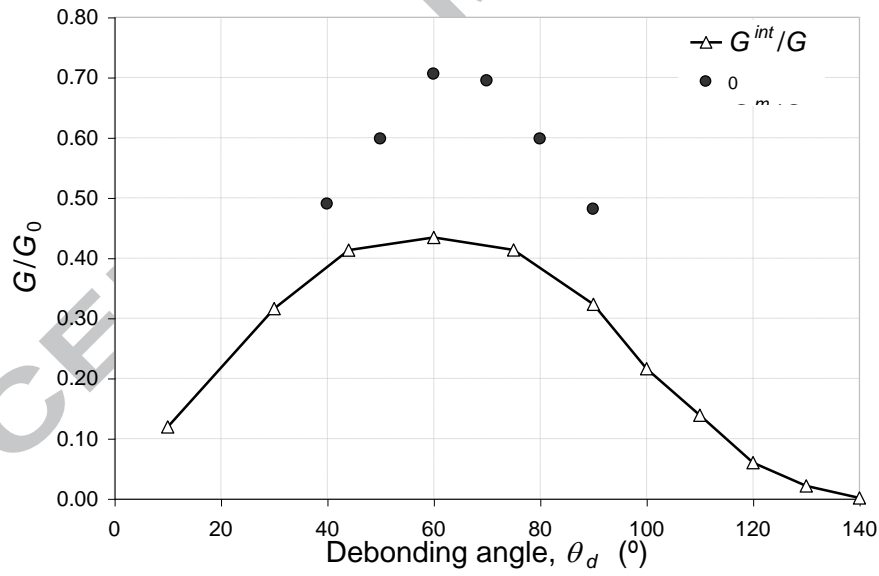


Fig. 8. Comparison between G^m and G^{int} ($\Delta T = -80^\circ\text{C}$ case). Glass fibre system.

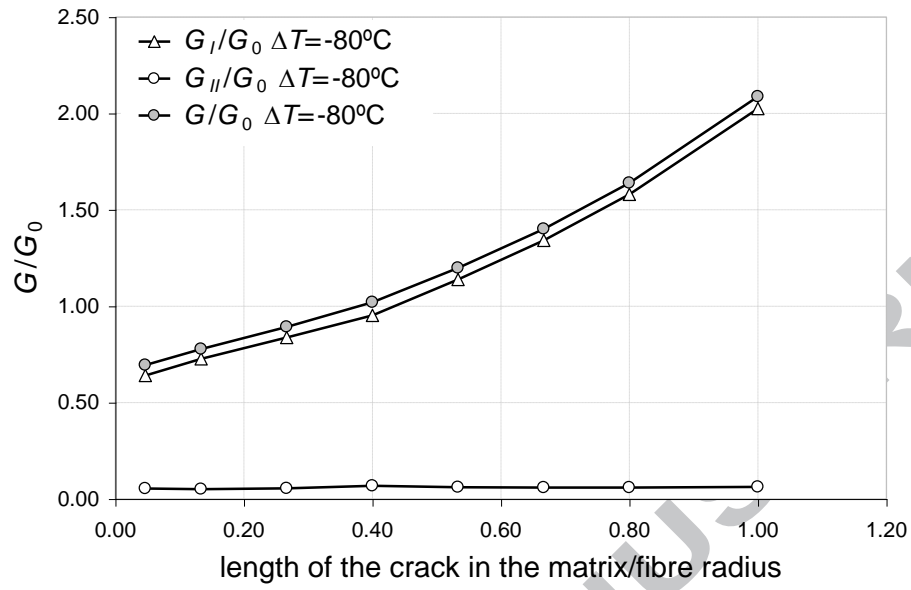


Fig. 9. Energy release rate for the crack in the matrix ($\theta_d = 70^\circ$). Glass fibre system.

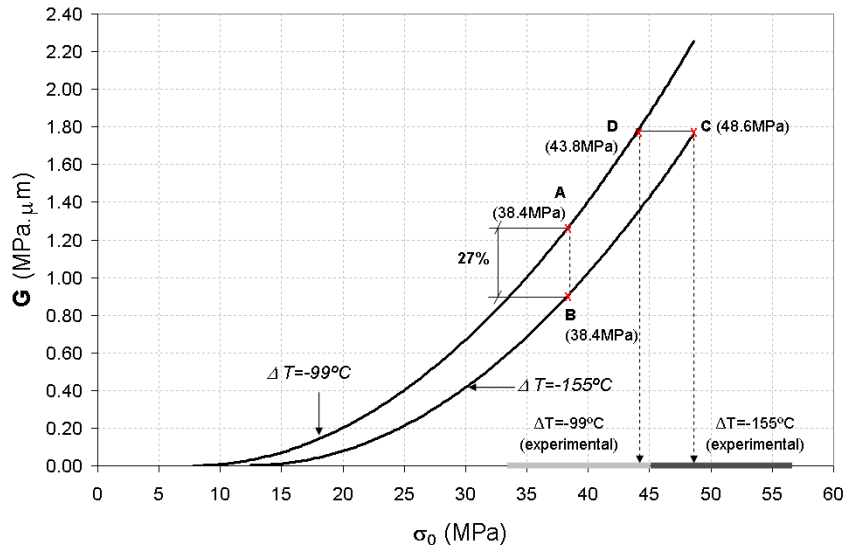


Fig.10. $G - \sigma_0$ evolutions associated to $\theta_d = 10^\circ$ for $\Delta T = -155^\circ\text{C}$ (curing cycle 1) and $\Delta T = -99^\circ\text{C}$ (curing cycle 2).

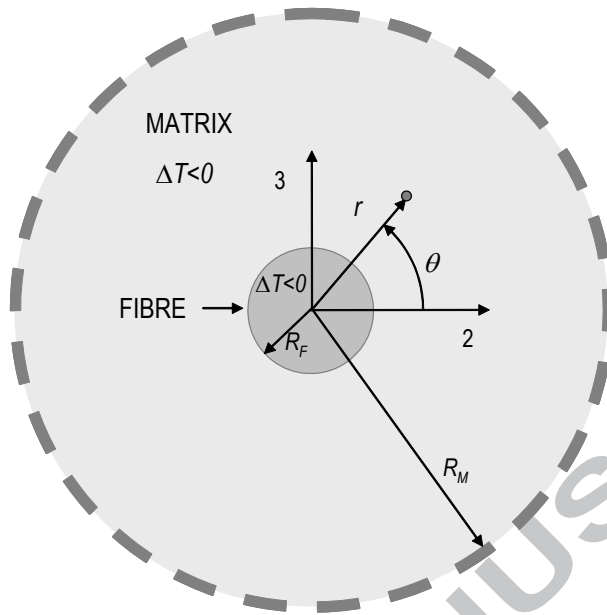


Fig. A.1. Single fibre embedded in an infinite matrix.

Material	Poisson coefficient	Young modulus	Coefficient of thermal expansion
Matrix (epoxy)	$\nu^m = 0.33$	$E^m = 2.79 \times 10^3 \text{ MPa}$	$\alpha^m = 52 \times 10^{-6} \text{ }^\circ\text{C}^{-1}$
Fibre (glass)	$\nu^f = 0.22$	$E^f = 7.08 \times 10^4 \text{ MPa}$	$\alpha^f = 7 \times 10^{-6} \text{ }^\circ\text{C}^{-1}$
Fibre (graphite)	$\nu^f = 0.20$	$E^f = 1.30 \times 10^4 \text{ MPa}$	$\alpha^f = 10^{-5} \text{ }^\circ\text{C}^{-1}$

Table 1: Thermoelastic properties of the materials.

Fig. 1. Micromechanical phases of inter-fibre failure under unidirectional tension.

Fig. 2. Single fibre modes: a) with interface crack only, and b) with interface kinked crack.

Fig. 3. G evolution versus θ_d ($\Delta T = 0^\circ \text{C}$ and $\Delta T = -80^\circ \text{C}$ cases). Glass fibre system.

Fig. 4. Contact zone evolution ($\Delta T = 0^\circ \text{C}$ and $\Delta T = -80^\circ \text{C}$ cases). Glass fibre system.

Fig. 5. $\psi_K(G)$ evolution ($\Delta T = -80^\circ \text{C}$ and $\Delta T = 0^\circ \text{C}$ cases). Glass fibre system.

Fig. 6. G and G_c for the interface crack ($\Delta T = -80^\circ \text{C}$). Glass fibre system.

Fig. 7. $\sigma_{\theta\theta}$ distribution around interface crack tip ($\Delta T = -80^\circ \text{C}$ case). Glass fibre system.

Fig. 8. Comparison between G^m and G^{int} ($\Delta T = -80^\circ \text{C}$ case). Glass fibre system.

Fig. 9. Energy release rate for the crack in the matrix ($\theta_d = 70^\circ$). Glass fibre system.

Fig. 10. $G - \sigma_0$ evolutions associated to $\theta_d = 10^\circ$ for $\Delta T = -155^\circ \text{C}$ (curing cycle 1) and $\Delta T = -99^\circ \text{C}$ (curing cycle 2).

Fig. A.1. Single fibre embedded in an infinite matrix.

Table 1: Thermoelastic properties of the materials.

Material	Poisson coefficient	Young modulus	Coefficient of thermal expansion
Matrix (epoxy)	$\nu^m = 0.33$	$E^m = 2.79 \times 10^3 \text{ MPa}$	$\alpha^m = 52 \times 10^{-6} \text{ }^\circ\text{C}^{-1}$
Fibre (glass)	$\nu^f = 0.22$	$E^f = 7.08 \times 10^4 \text{ MPa}$	$\alpha^f = 7 \times 10^{-6} \text{ }^\circ\text{C}^{-1}$
Fibre (graphite)	$\nu^f = 0.20$	$E^f = 1.30 \times 10^4 \text{ MPa}$	$\alpha^f = 10^{-5} \text{ }^\circ\text{C}^{-1}$

Figure1

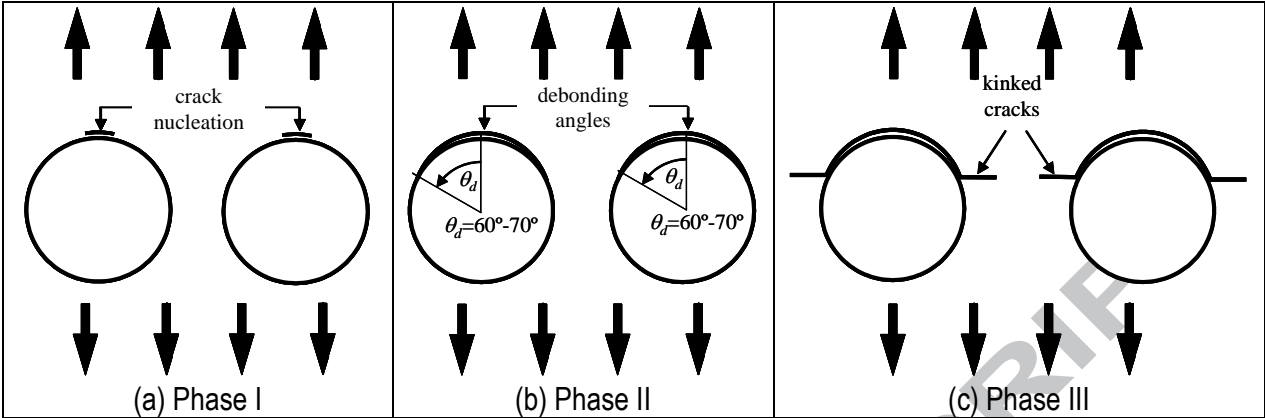


Figure2

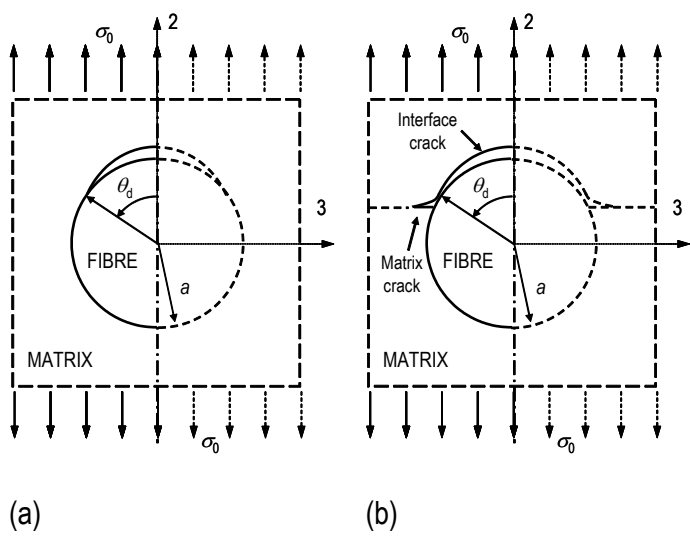


Figure3

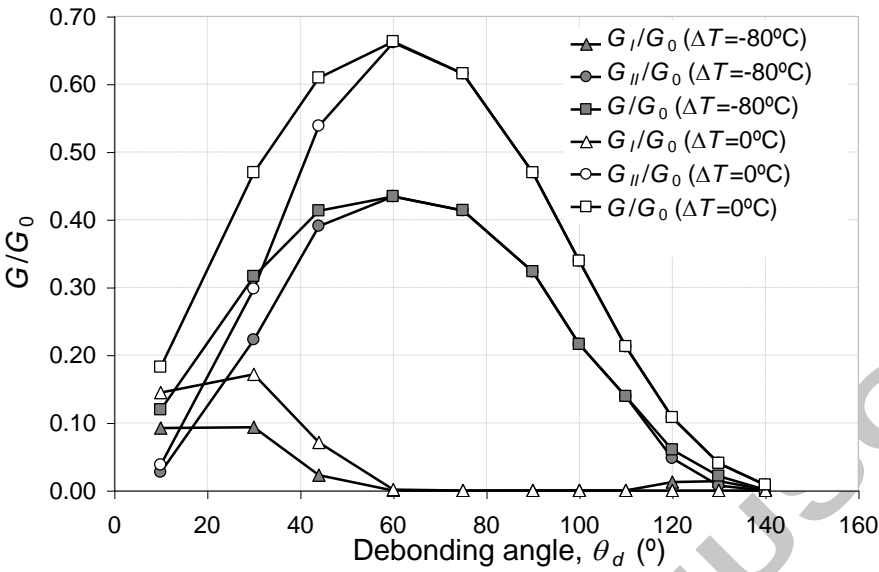


Figure4

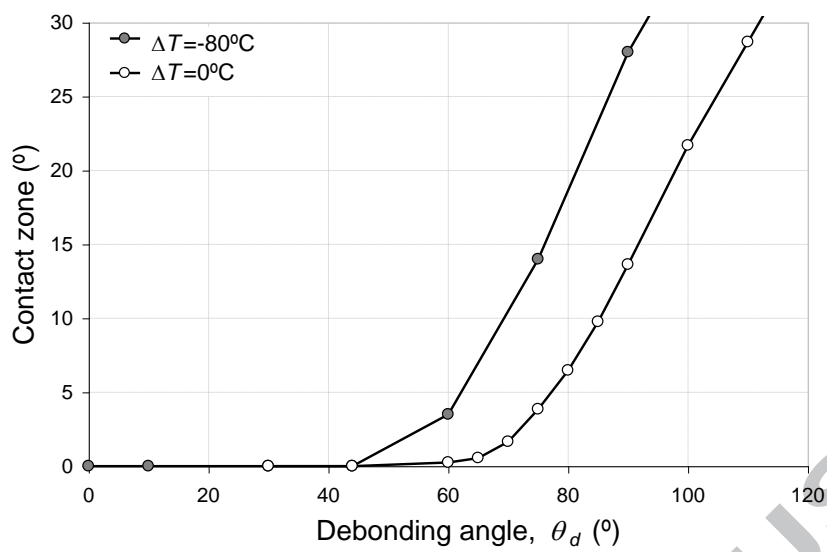


Figure5

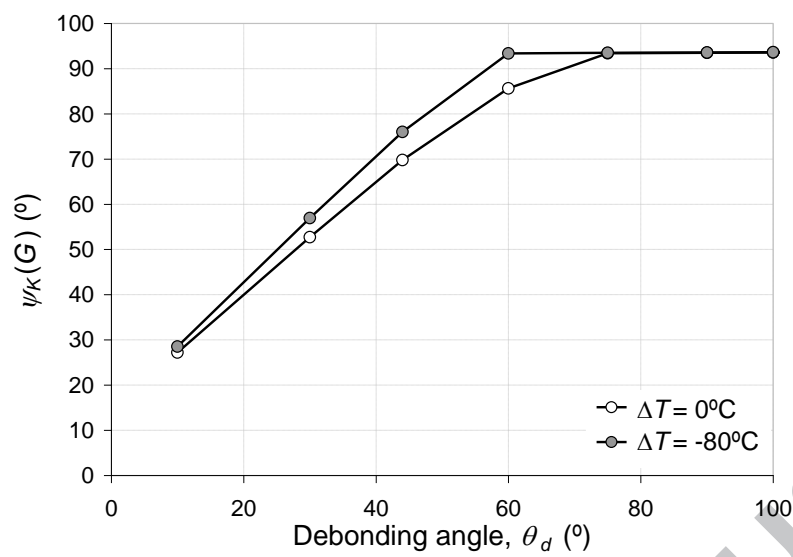
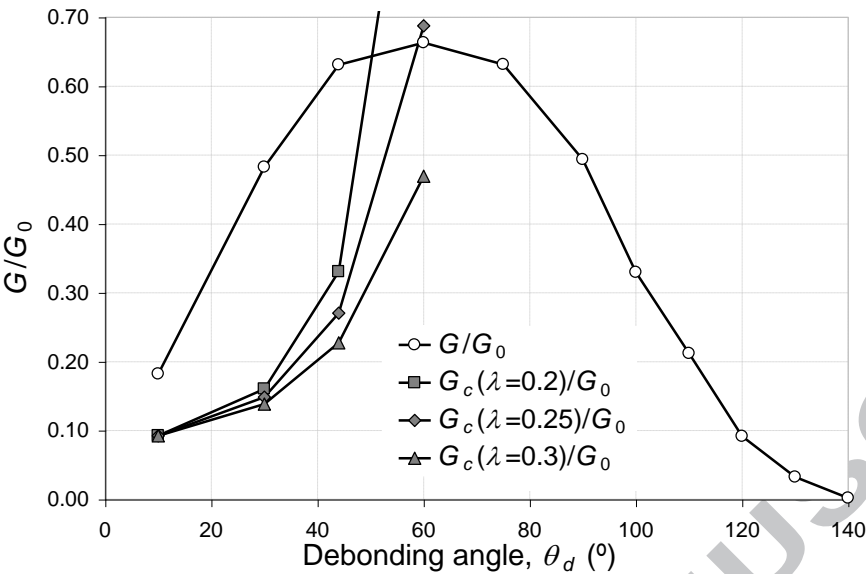


Figure6



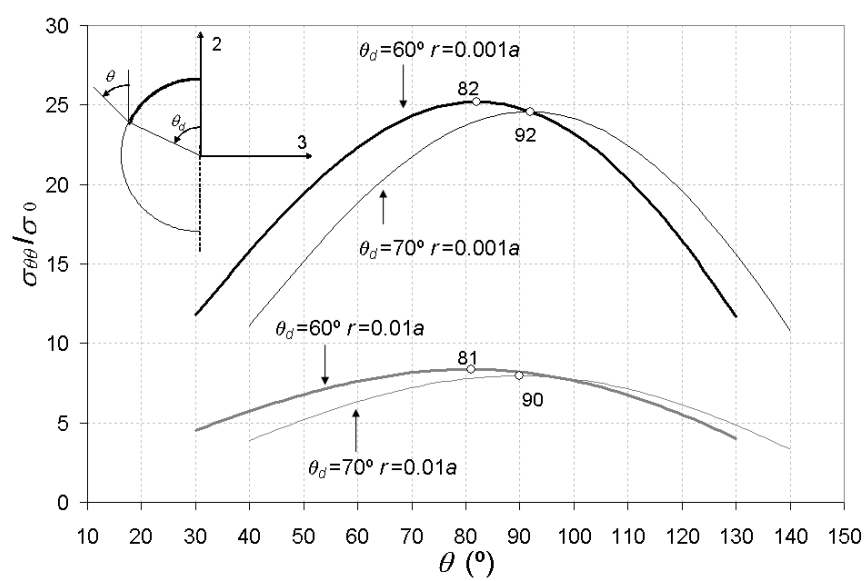


Figure8

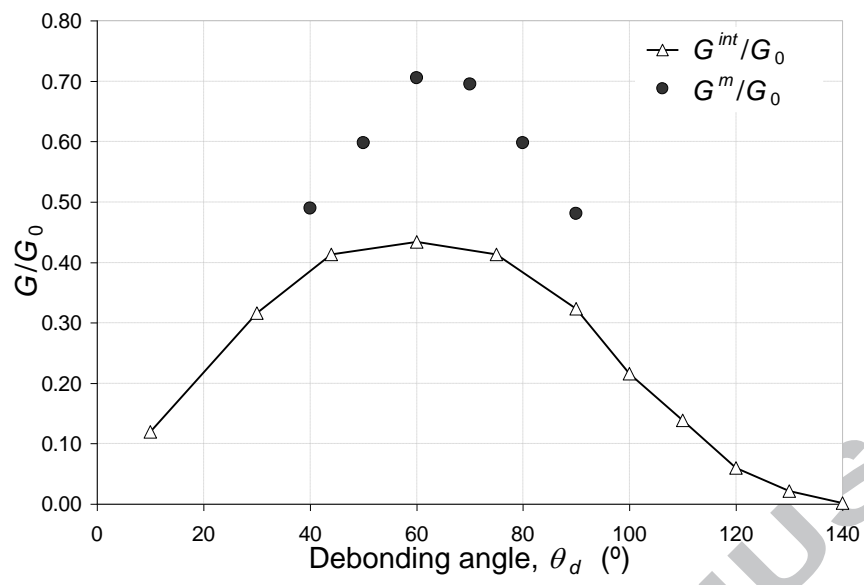


Figure9

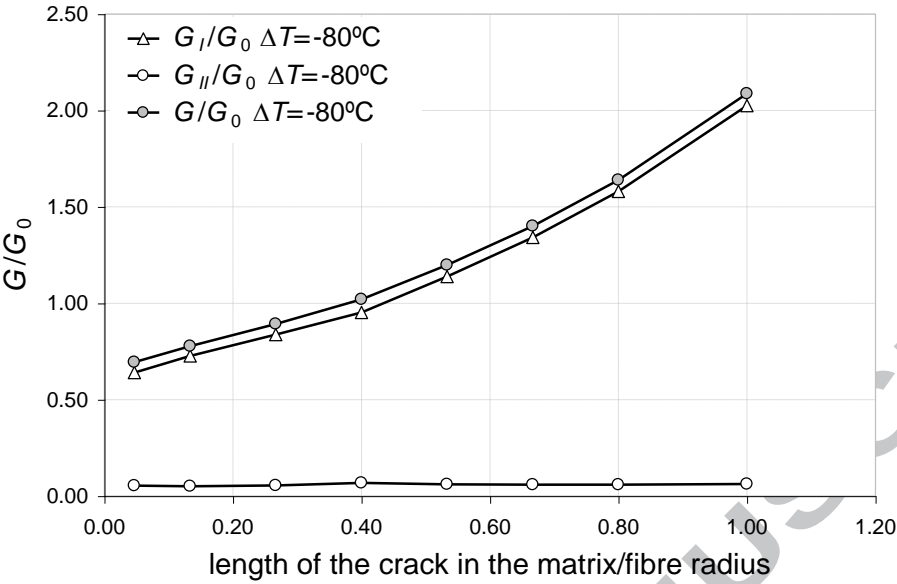


Figure10

